Tilting process with humidity: DEM modeling and comparison with experiments

Luc Oger, Ana M. Vidales, Rodolfo O. Uñac & Irene Ippolito

Granular Matter

ISSN 1434-5021
Volume 15
Number 5

Granular Matter (2013) 15:629-643
DOI 10.1007/s10035-013-0433-9

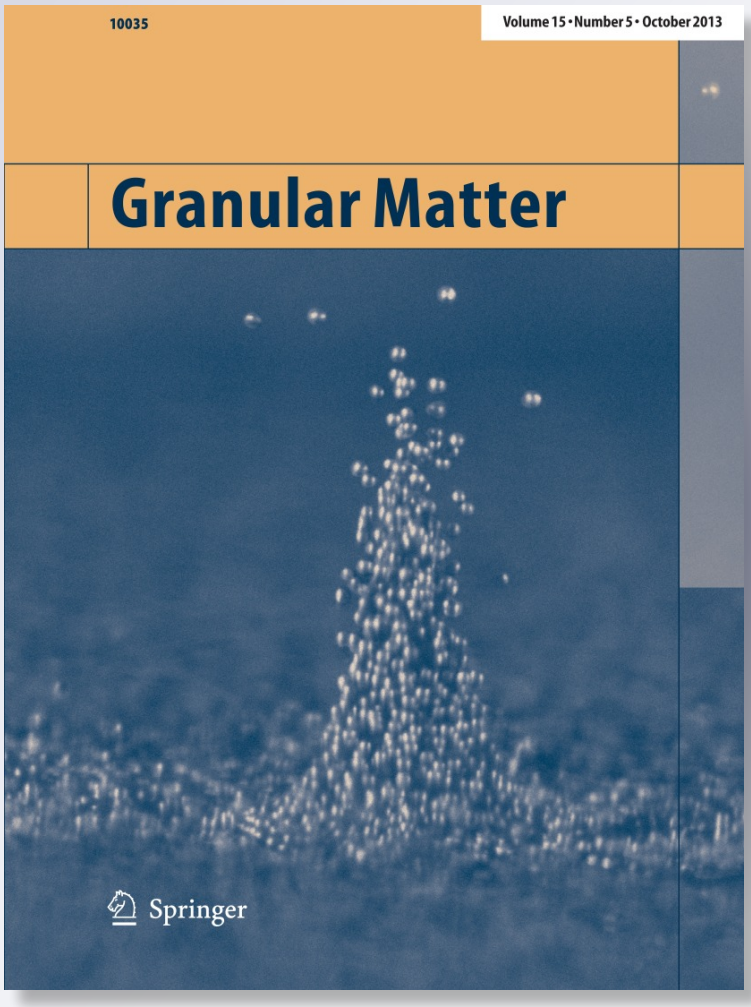

Springer

Granular Matter (2013) 15:629–643
DOI 10.1007/s10035-013-0433-9

ORIGINAL PAPER

Tilting process with humidity: DEM modeling and comparison with experiments

Luc Oger · Ana M. Vidales · Rodolfo O. Uñac · Irene Ippolito

Received: 17 December 2012 / Published online: 10 July 2013

Abstract Granular matter is present everywhere in our practical lives and mostly used in natural environment (i.e. classical atmospheric conditions). This fact implies that the humidity rate which controls the water content can be involved in their behaviors. Especially adhesion forces between grains are linked to this humidity rate. Here we study a well known experiment defined as a laboratory test for avalanches. We continuously tilt a box filled with grains up to the appearance of precursors and full avalanches. These avalanches are directly proportional to the forces acting at the contact level between grains. We use a numerical approach based on the classical discrete element methods 'spring-Dashpot' with soft model. Firstly, we check the ability of our code to handle tilting experiments, then, an extra adhesion term linked to the humidity rate is added. Full comparison between 'dry' case and humid case is done.

L. Oger (✉)
Institut de Physique de Rennes, Université de Rennes1,
263, Avenue du General Leclerc, Campus de Beaulieu,
CS 74205, 35042 Rennes Cedex, France
e-mail: luc.oger@univ-rennes1.fr

A. M. Vidales · R. O. Uñac
Laboratorio de Medios Granulares, INFAP-CONICET,
Universidad Nacional de San Luis, Ejército de los Andes 950,
D5700HHW San Luis, Argentina
e-mail: avidales@unsl.edu.ar

R. O. Uñac
e-mail: runiac@unsl.edu.ar

I. Ippolito
Grupo de Medios Porosos, Facultad de Ingeniería,
Universidad de Buenos Aires, Av. Paseo Colón 850,
C1063ACV Buenos Aires, Argentina
e-mail: iippoli@fi.uba.ar

Keywords Granular instabilities · Humidity · DEM code · Inclination

1 Introduction

Handling granular media is one of the most energy consuming reason for the industries around the world. This fact is due to several factors such as transporting along a long distance, mixing several sizes of grains or grains with different properties, crushing big rocks, sintering grains, and so on. These different processes involve the use of large external forces in order to move or break the grains, but these situations can be still more energy consuming if some adhesion forces between the grains are also present and have a very strong influence such as the humidity effect. In some countries, such as Norway or Argentine, where some of the authors are working, the humidity rate can reach 100 % in some regions and can stand during several days or weeks. This is one of the main reasons of our involvement in this study. In this paper, we will present, first the experimental data obtained in Buenos Aires by Gómez [1]. Then we will collect the different descriptions or assumptions about the adhesion forces due to humidity. In the following section, we will describe our DEM model to handle classical tilting modeling for analyzing precursors and avalanches. Finally, some preliminary results obtained when the capillary forces are modeled only by single bridges between two spheres are presented.

2 State of the art

2.1 Recollection of the basic theory available for humidity interaction

In any natural environment, we are always dealing with humidity with rate values varying from few percent up to

one hundred percent. This humidity factor is directly linked to the water presence in the air. It is well known that cohesion in wet granular materials depends on the amount of liquid in the system. The following four regimes of liquid content, ordered by an increasing amount of water, have been distinguished in wet granular media (see for example [2]):

- **Pendular state**: Particles are held together by liquid bridges at their contact points.
- **Funicular state**: Some pores are fully saturated by liquid, but there still remain voids filled with air.
- **Capillary state**: All voids between particles are filled with liquid, but the surface liquid is drawn back into the pores under capillary action.
- **Slurry state**: Particles are fully immersed in liquid and the surface of liquid is convex, i.e. no capillary action is present at the surface.

In the first situation, we can describe the resulting normal force acting at each contact between two spheres as the sum of a repulsive force f_n^r and an attractive capillary force f_n^c. This capillary force is a function of the liquid bridge bonding the two spheres, and its amplitude, when the two spheres are in contact (gap distance $\delta = 0$) does not depend on the volume of this bond but only on the liquid surface tension, γ_{lv}, the wetting angle of liquid vapor, θ, and the radii of the two spheres. Consequently, when the overlap between two spheres ($\delta \leq 0$) can be considered small compared to their diameters, the amplitude of the capillary force f_0 is equal to [3]:

$$f_0 = -\kappa R \tag{1}$$

where R is the sphere radius assuming both spheres having the same radius or some average value if the two spheres are not identical, and κ is equal to

$$\kappa = 2\pi\gamma_s \cos(\theta), \tag{2}$$

where γ_s is the wetting surface tension for the solid and $\cos(\theta)$, defined from the wetting angle, is around 0.84 for water on glass. Note that f_0 in Eq. (1) is independent of the volume of the liquid bridge, V_b. By definition, the adhesion force f_0 at contact (i.e. $\delta = 0$) is the highest value of the capillary force. It is assumed that this force declines as the gap δ increases positively.

The decreasing of the capillary force is a key parameter and strongly varies depending of the possible approaches available in the literature. One of the first classical approach is a standard exponential decay, where δ ranges from 0 up to a maximal value δ_{max}. The exponential decay and this last value δ_{max} are, for example, defined by Richefeu et al. [4]. Below in Sect. 5.1, we will summarize and use the approach defined by Charlaix et al. [5] which consider a simple linear decrease for the capillary force. In their analysis, the maximal capillary forces and the slopes vary according to the humidity rates.

2.2 Summary of experimental results

Many of the experimental studies on granular media, specially those related to the physics field, are devoted to dry granular materials, i.e. where the effect of interstitial fluids can be neglected or, at least, modified in order to avoid the consequences of its presence. This assumption is naturally not valid, especially when the grain diameters are small (less than 200–300 μm). But only recently, some authors have developed new techniques to carefully analyze the 'complementary' force effect that appears when humidity is present in the system. Here, we will describe a series of these experimental results, some of which will be used in our present study to validate our model.

2.2.1 'Static' humidity measurements

Recently, Herminghaus et al. [6,7] have presented a large review on the dynamics of wet granular matter. They extended the classical four regimes model up to a fifth model by separating the low humidity case in two different cases (case I is for asperity water content, II is for water at the contact), the three other regimes remain identical: III = pendular; IV = funicular; V = immerged). They introduced also the dynamical aspect of the water propagation inside the porous structure. Iveson et al. [8] have studied the evolution of the granulation of grains by increasing the liquid content, water or other liquid binder. The strength of the final pellet is directly linked to the liquid properties and to the amount of liquid present between grains. They also demonstrated the time evolution of the granulation linked to the humidity aging effect.

Hornbaker et al. [9,10] have also measured the evolution of the angle of repose and its distribution with the oil-layer thickness. Tegzes et al. [11] have also studied liquid induced transition for granular media. They have observed the direct link between the angle of repose and the oil thickness for different container diameters and the increase of its standard deviation again with the oil thickness. In another point of view, Kohonen et al. [10] have correlated the increase of the number of liquid bridges per bead (or active contacts) with the increase of the liquid content. They demonstrate also the importance of the time needed to let the liquid penetrating the grain contact structure: increase of liquid volume during hours of experiments. So, we can deduce that the humidity rate controls the liquid thickness and by consequence modify the angle of repose by changing the number of contacts in the phases I and II defined previously. Knowledge of the amount of liquid at which these changes arise is a key input parameter when humidity effects are present in a system.

In this sense, Forny et al. [12] have measured the water sorption isotherm for the case of a small packing of glass beads with average diameter of 85 μm. In their work, they found that, up to 70 % humidity rate there is only a slow increase in the amount of water adsorbed inside the packing. So, during this stage, one can assume that the system remains in a pendular regime (i.e. water is present only at the contact points). This assumption can help us to model the humidity effect through the presence of liquid bridges, responsible of the adhesion forces. This modeling will be described later on in this paper (Sect. 5.1).

In the last decades, Charlaix et al. [3,13–16] have made a series of contact experiments to measure the capillary forces and its aging effect in very well controlled experimental setup. More recently, Charlaix et al. [3,5,17] have proposed an analytic expression for the behaviour of the adhesion force between two spheres as a function of their gap. They found that their expression allowed to calculate two main aspects of that behaviour: the disjoining pressure (calculated from the slope of the linear part of the variation of the force with the gap), and the estimation of the solid-liquid-vapor interaction potential (calculated from its maximum amplitude at distance $\delta = 0$). This expression will be used in our model, as it will be explained later on.

2.2.2 *Avalanche measurements with humidity effects*

Gómez [1,18] carried out a lot of experiments using granular materials under the presence of well controlled relative humidity. More recently, they carried out experiments to measure the maximum angle of stability and the repose angle after an avalanche, with glass beads confined in a tilting box. In their experiments, they used spheres with a density of 2.5 g/cm^3 and different size diameters (0.5, 1, 2 mm). They used two different sizes for the boxes: (6.0 × 6.5 × 11.0) cm^3 and (5.0 × 6.5 × 10.3) cm^3, which guarantee a good statistics, as the system has enough grains in each direction. Once the box was filled with the grains and the top surface flatten with a flat tool, a duration of two weeks at a given relative humidity rate is waited in order to homogenize the humidity in all the sample. Then, a tilting process began until an avalanche occurred. At this stage, the maximum angle of inclination and the angle of repose (angle at which the surface relaxed after the avalanche stops) were measured. Then, the box was kept in repose for ten minutes until a new tilting process began, and so on. They have waited until two hours between avalanches to see if the time evolution mentioned in the previous reference [10] are still significant in their experiments without a big effect. Some of the results of these experiments are reproduced from [1] in Fig. 1 for a better comparison with our results described later on. The maximum inclination angle after the first avalanche and the repose angle for the surface of the packing of grains of 1 mm are plotted against the humidity rate (from 5 up to 90 %). It is clear from Fig. 1 that the maximum angle increases with the humidity rate, especially for values higher than 70 %. This behavior can be compared with the results shown by Forny et al. [12] where, up to 70 % of humidity rate, a small increase of the water content inside the bead packing is observed and a fast increase after that. In this way, we can assume that, in both cases, the pendular state can be used as an actual situation and we will use this assumption in our simulations.

By pursuing the experiments after the first avalanche, Gómez [1] obtained results reproduced also in Fig. 2 which presents the difference between the maximum angle of stability and the repose angle after each avalanche (first and successive ones) versus the humidity rate (from 5 up to 90 %), for different bead sizes. Here, Gómez [1] demonstrated that a big difference exists between the first avalanche behavior and the following successive ones. This can be interpreted as a non homogeneous history for producing the initial configuration of the packing, especially in the upper layers on its surface: flattened and may be compacted during the packing construction. These inhomogeneous arrangements disappear after the first avalanche, when a new surface is obtained as a result of the previous avalanche and the following avalanches

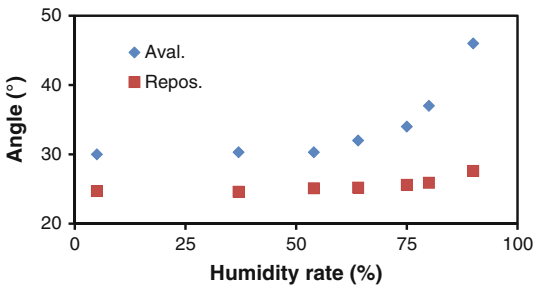

Fig. 1 Measures of the maximum angle of stability and the repose angle after the first avalanche for grains of 1 mm, as a function of the humidity rate (from 5 up to 90 %) extracted from [1]

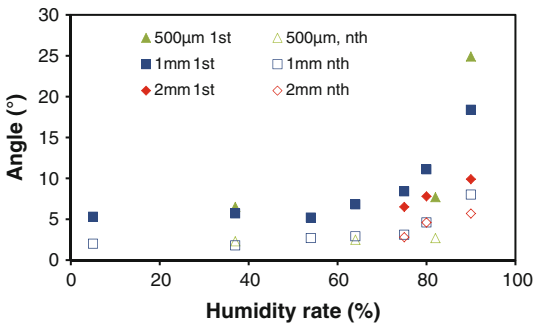

Fig. 2 Measures of the difference between the avalanche angle (maximum angle of stability) and the repose angle for the first avalanche and the successive ones (nth) as a function of the humidity rate (from 5 up to 90 %), for the three different grain sizes used in his experiments (500 μm, 1, 2 mm)

are almost reproducible. We will also use this feature in the analysis of our numerical results.

2.3 Overview of previous numerical results

Lian et al. [19] have developed the first model which integrates capillary forces for the simulation of wet granular assemblies in the pendular state, using a soft particle DEM approach code. They estimated the viscous force in the normal direction of approach of the two agglomerates of particles through a rigid sphere solution. Computer simulations were performed for a number of collinear collisions between the two agglomerates. For all values of the relative impact velocity and fluid viscosities, the two agglomerates always coalesced. They interpreted that the main mechanism for the kinetic energy dissipation is due to the viscous resistance of the interstitial fluid. Thus, the resulting attenuation of the stored elastic energy was the responsible for the agglomerate coalescence.

Dong et al. [20,21] present an experimental and numerical study of the settling of uniform spheres in liquids. In their model, the buoyancy, drag, and Magnus' lift forces are also included in addition to the contact and van der Waals forces. The diameter range for the beads used in their work is partially the same as the one used here. As in a previous work [22], they confirmed that interparticle forces play a critical role in forming the so-called random loose packing (RLP) and, more generally, in the piling process. Taken this into account, one should use a different approach whether the packing has been built with or without the presence of humidity. In our study, as in Gómez's experiments, the packings were built in a dry environment during the complete piling process, then the effect of humidity is added or allowed to be present.

Richefeu et al. [4,23] compared the probability density functions of normal forces in dry and wet granular systems from 3D simulations by DEM codes either using molecular dynamic or contact dynamic methods. First, they performed basic experiments with sand grains and glass beads with different size distributions. They showed that the yield loci in all cases and for several levels of water content, were well fitted by a straight line, in agreement with the Mohr-Coulomb model with cohesion. They found that the cohesion term increases non linearly with the water content. In their numerical model, they used the classical exponential decay described by Richefeu et al. and Soulié et al. [4,24] where the largest absolute value f_0 of the capillary force has the same definition as in Eq. (1). Their numerical results are consistent with the behaviour for the Coulomb cohesion versus water content. They also demonstrated that the weak compressive bonds are almost isotropically distributed whereas strong compressive and tensile bonds had a pronounced anisotropy. This anisotropy could affect a gravity driven tilting process like the one studied in the present work.

Anand et al. [25] investigated the parameters affecting the discharge rate of a wet cohesive system from a quasi-3-D, rectangular hopper using the DEM with molecular dynamics method. They also used an exponential decay for the cohesion force taken from Mikami et al. [26] which is, in fact the original version of the formula used by Richefeu et al. and Soulié et al. [4,24]. In their simulations, the normal contact force was calculated using the classical ratchet model developed by Walton and Braun [27]. Some of the assumptions used in [25] can be easily extended to our present study. Those assumptions are:

- the total liquid content of the system is distributed so that every particle has a constant thickness of liquid around it;
- when two particles come into contact, a liquid bridge is formed between them;
- when particles are in an enduring contact, a Hookean spring force, a Coulombic friction force, and an attractive cohesive liquid bridge force act on the particles;
- the magnitude of the cohesive force remains constant during the contact;
- when particles are separating after a contact, only gravity and a liquid bridge force act in the normal direction.

They observed that the influence of liquid content depends on the Bond number. At low Bond number, identical discharge rates were obtained despite varying liquid content over a wide range. This result confirms that low humidity rate has no considerably effect on the behaviour of a granular flow, the fact that will be observed in our present work.

3 Our DEM numerical model and its setup

In order to model the experiments made by Gómez [1], we are using a classical DEM molecular dynamics model known also as soft spheres (i.e. spheres can overlap). The present model follows the two-dimensional formulation of Savage [28] and the three-dimensional extension used by Oger et al. [29]. The particles are modeled as spheres. A "soft-particle" approach is used, where each sphere can have multiple contacts that can persist for extended durations (typically during 50 time steps). Both normal and tangential forces develop at the contact between two spheres. When only compressive forces are allowed, the simulations represent dry, non-cohesive particles assemblies. Allowing tensile forces at the contacts (normal or global) modelize wet, cohesive particles for the already colliding particles. No long range interactions are present in this model.

3.1 Contact between particles

The *i*th particle is characterized by its radius R_i, the position of its centre (x_i, y_i, z_i) and the rotation θ_i around its centre. Without cohesive forces, a contact takes place only when two spheres overlap. When contact occurs between two particles, normal and tangential forces increase as the centres of the particles approach each other.

We start the description with conditions where no tensile force is present. The normal force F_n at the contact is modeled as viscoelastic. It consists of an elastic (a linear spring) contribution and viscous damping (a linear dashpot) contribution as follows:

$$\begin{array}{ll} compression: & F_n = k_n\delta - b_n v_n \\ tension: & F_n = 0 \end{array} \tag{3}$$

where k_n is the spring constant for normal forces, δ is the relative normal displacement, v_n is the relative normal velocity, and b_n is the dashpot constant for normal forces. The dashpot term b_n is naturally linked to the restitution coefficient of the grains by

$$b_n = -\log(e) * 2.0 * \frac{\sqrt{k_n}}{\sqrt{log^2(e) + \pi^2}}; \tag{4}$$

with e the restitution coefficient. The tangential force, F_t is calculated according to a Coulomb friction law:

$$F_t = \mu F_n \tag{5}$$

where μ is the coefficient of friction which can be related to the intergranular friction angle (ϕ_u) by $\mu = \tan(\phi_u)$. The tangential force acts in a direction opposite to that of the relative tangential velocity v_t.

In absence of body force, each particle is in static equilibrium under the action of contact and external forces. The state equations of the *i*th particle are:

$$\begin{aligned} &\sum_{j=1}^{n_c^i} F_x^{j,i} = f_x^i \\ &\sum_{j=1}^{n_c^i} F_y^{j,i} = f_y^i \\ &\sum_{j=1}^{n_c^i} F_z^{j,i} = f_z^i \\ &R_i \sum_{j=1}^{n_c^i} \left(F_x^{j,i} n_y^{j,i} - F_y^{j,i} n_x^{j,i} \right) = f_\theta^i \\ &R_i \sum_{j=1}^{n_c^i} \left(F_x^{j,i} n_z^{j,i} - F_z^{j,i} n_x^{j,i} \right) = f_\phi^i \end{aligned} \tag{6}$$

where n_c^i is the number of contacts on the *i*th particle, $F_x^{j,i}$, $F_y^{j,i}$ and $F_z^{j,i}$ are the x, y and z components of the *j*th contact force acting on the *i*th particle and f_x^i, f_y^i, f_z^i and f_θ^i, f_ϕ^i are the x, y, z and θ, ϕ component respectively, of the external forces of the *i*th particle.

The x, y and z coordinates of the *i*th particle at time step N are obtained as

$$\begin{aligned} x_i^{(N)} &= x_i^{(N-1)} + \Delta t * v_x^{i,(N-1)} + \tfrac{1}{2}\Delta t^2 * f_x^{i,(N-1)} \\ y_i^{(N)} &= x_i^{(N-1)} + \Delta t * v_y^{i,(N-1)} + \tfrac{1}{2}\Delta t^2 * f_y^{i,(N-1)} \\ z_i^{(N)} &= z_i^{(N-1)} + \Delta t * v_z^{i,(N-1)} + \tfrac{1}{2}\Delta t^2 * f_z^{i,(N-1)} \\ v_x^{i,(N-\frac{1}{2})} &= v_x^{i,(N-1)} + \tfrac{1}{2}\Delta t * f_x^{i,(N-1)} \\ v_y^{i,(N-\frac{1}{2})} &= v_y^{i,(N-1)} + \tfrac{1}{2}\Delta t * f_y^{i,(N-1)} \\ v_z^{i,(N-\frac{1}{2})} &= v_z^{i,(N-1)} + \tfrac{1}{2}\Delta t * f_z^{i,(N-1)} \\ \theta_i^{(N-\frac{1}{2})} &= \theta_i^{(N-1)} + \tfrac{1}{2}\Delta t * \omega_i^{(N-1)} \\ \omega_i^{(N-\frac{1}{2})} &= \omega_i^{(N-1)} + \tfrac{1}{2}\Delta t * \tfrac{\partial \omega_i}{\partial t}^{(N-1)} \\ \phi_i^{(N-\frac{1}{2})} &= \phi_i^{(N-1)} + \tfrac{1}{2}\Delta t * \psi_i^{(N-1)} \\ \psi_i^{(N-\frac{1}{2})} &= \psi_i^{(N-1)} + \tfrac{1}{2}\Delta t * \tfrac{\partial \psi_i}{\partial t}^{(N-1)} \end{aligned} \tag{7}$$

then the calculation of the new forces f_x^i, f_y^i and f_θ^i are performed for the new state of the system using the set of Eq. (6). After this operation a final update is realized to end the timestep (N):

$$\begin{aligned} v_x^{i,(N)} &= v_x^{i,(N-\frac{1}{2})} + \tfrac{1}{2}\Delta t * f_x^{i,(N)} \\ v_y^{i,(N)} &= v_y^{i,(N-\frac{1}{2})} + \tfrac{1}{2}\Delta t * f_y^{i,(N)} \\ v_z^{i,(N)} &= v_z^{i,(N-\frac{1}{2})} + \tfrac{1}{2}\Delta t * f_z^{i,(N)} \\ \theta_i^{(N)} &= \theta_i^{(N-\frac{1}{2})} + \tfrac{1}{2}\Delta t * \omega_i^{(N-\frac{1}{2})} \\ \omega_i^{(N)} &= \omega_i^{(N-\frac{1}{2})} + \tfrac{1}{2}\Delta t * \tfrac{\partial \omega_i}{\partial t}^{(N-\frac{1}{2})} \\ \phi_i^{(N)} &= \phi_i^{(N-\frac{1}{2})} + \tfrac{1}{2}\Delta t * \psi_i^{(N-\frac{1}{2})} \\ \psi_i^{(N)} &= \psi_i^{(N-\frac{1}{2})} + \tfrac{1}{2}\Delta t * \tfrac{\partial \psi_i}{\partial t}^{(N-\frac{1}{2})} \end{aligned} \tag{8}$$

3.2 Tensile strength

In our model, we can also introduce bonds between spheres that are in contact at some initial stage of the packing. This condition represents an assembly of particle with tensile strength between them. This tensile strength can be "generated" by the surface tension of the liquid between contacts as described later on. In that case, the normal force is calculated using the first expression of Eq. 3 and is allowed to have tensile values (i.e. negative value) up to the value of the tensile strength defined for this bond. If the normal tensile force exceeds the tensile strength, the bond breaks, then the normal force follows the classical rule of Eq. 3 (i.e. positive value).

The force in the tangential direction is modeled as viscoelastic below the tensile strength limit; a linear spring and a linear dashpot are used as follows

$$F_t = k_t \delta_t - b_t v_t \tag{9}$$

where k_t is the spring constant for tangential forces, δ_t is the relative lateral displacement, v_t is the relative tangential velocity, and b_t is the dashpot constant for tangential forces. The tangential force, F_t is also submitted to a critical value which is chosen equal to the tensile strength; if the tangential force exceeds this tensile strength, the bonds breaks and the tangential force follows the Mohr Coulomb law defined in Eq. 5.

3.3 Nondimensional approach

It is convenient to cast the governing Eqs. (3) and (9) in nondimensional form and to perform the computations based upon these dimensionless equations [28,29]. It is straightforward to revert back to physical variables if desired, but in using the nondimensional form of the equations we have the advantage of being able to easily recover results for different physical scales (fine powders of 10 μm up to ice floes of 100 km). Hence, all lengths are nondimensionalized by D, the diameter of the largest sized particles used in the computations. Time is nondimensionalized by dividing by $\sqrt{\frac{M}{K}}$, where M is the mass of the largest particle and K the effective spring constant used in Eq. 3. Velocities are nondimensionalized by dividing by $\frac{D}{\sqrt{\frac{M}{K}}}$. Thus we introduce the following nondimensional time and spatial coordinates

$$(\tilde{t}, \tilde{x}, \tilde{y}, \tilde{z}) = \left(t\sqrt{\frac{K}{M}}, \frac{x}{D}, \frac{y}{D}, \frac{z}{D} \right). \tag{10}$$

The dimensionless velocity components and the dimensionless angular velocity are defined as

$$\left(\tilde{v}_x, \tilde{v}_y, \tilde{v}_z, \tilde{\omega}, \tilde{\psi}\right) = \sqrt{\frac{M}{K}} \left(\frac{v_x}{D}, \frac{v_y}{D}, \frac{v_z}{D}, \omega, \psi\right). \tag{11}$$

Rewriting Eqs. (3, 9) in terms of the nondimensional variables (10, 11) we obtain

$$\begin{aligned}
\frac{d\tilde{v}_x}{d\tilde{t}} &= \sum_{i=1}^{n_c^i} \frac{\tilde{k}}{4\tilde{r}^2} (\tilde{\delta}_i)_x \\
\frac{d\tilde{v}_y}{d\tilde{t}} &= \sum_{i=1}^{n_c^i} \frac{\tilde{k}}{4\tilde{r}^2} (\tilde{\delta}_i)_y \\
\frac{d\tilde{v}_z}{d\tilde{t}} &= \sum_{i=1}^{n_c^i} \frac{\tilde{k}}{4\tilde{r}^2} (\tilde{\delta}_i)_z \\
\frac{d\tilde{\omega}}{d\tilde{t}} &= \sum_{i=1}^{n_c^i} sign_{ij} \mu \frac{\tilde{k}\tilde{\delta}_i}{2\tilde{r}^3} \\
\frac{d\tilde{\psi}}{d\tilde{t}} &= \sum_{i=1}^{n_c^i} sign_{ik} \mu \frac{\tilde{k}\tilde{\delta}_i}{2\tilde{r}^3}
\end{aligned} \tag{12}$$

where $\tilde{\delta} = \frac{\delta}{D}$ and $\tilde{r} = \frac{r}{D}$ are the nondimensional distances and the dimensionless spring constant $\tilde{k} = \frac{k}{K}$. The terms $sign_{ij}, sign_{ik}$ specify the directions of the ith tangential contact force acting on this particle.

3.4 Initial preparation

The preparation of the sample is obtained by two consecutive procedures: a box filling step followed by the presence of a gravity field.

3.4.1 Piling of the grains

The box filling is partially defined as under gravity (directional effect) [30]. The first layer is made by touching spheres sitting on the bottom wall up to the maximal possible packing fraction when no reorganization is made. Then each new sphere is placed in a stable position when it has three underlying contacts. These ones are coming from the already placed spheres. The first one is chosen at random, then in its neighborhood for the two other ones. This procedure implies naturally that these three new contacts are close to the upper surface and the center of the new sphere is inside a given thin layer. So, in order to obtain a dense packing, we progress up slowly, layer by layer with a layer thickness of the order of 1/10th of the sphere radius. This Powell's algorithm will produce a dense packing fraction around $0.58 - 0.60$. The sample contains 16,000 spheres with a mean radius R defined as unity (for dimensionless purpose described in Sect. 3.3) and an uniform size dispersion σ chosen from 5 up to 15 %. The box has a square bottom with a dimension close to 54 times R and the height goes up to 40 times R. These ranges for the three dimensions of the box were chosen in accordance with the size of the experiments made by Gómez [1].

3.4.2 Gravity field

The second step consists of a switching of the gravity field to introduce the natural gravity gradient pressure through the full sample (linked to the classical known value: $\rho g h$ with ρ the grain density, g the gravity field and h the height of material on top). Of course this simple $\rho g h$ calculus is only valid if the height/width ratio is small enough to avoid the 'Janssen effect' [31] (i.e. pressure screening along the sample height) which is not the case in all the avalanche experiments. In the final stage of preparation, the packing has to reach an equilibrium obtained by slow displacements of the grains. These displacements can be checked by looking at the instantaneous velocities of all the particles inside the sample and by a global increase of the packing fraction. At the end of this process, all the instantaneous velocities have to be smaller than a given value but cannot be all together

equal to zero. Indeed, our DEM code is based on the standard Spring-Dashpot model which implies the persistence of small oscillations of the grains: they cannot be perfectly immobile in the DEM approach. But this contribution to the kinetic energy remains always small as the time step is also small (order of 1/50th of the collision time) for avoiding large overlaps during the displacement of the spheres. We can already notice that this fact will be also visible in the definition of the precursors of the avalanches in the rest of our paper.

3.4.3 Tilting of the box

After this long initial preparation procedure, we can start the tilting process of the sample. We achieve this by only doing a rotation of the gravity field at a given rate. In this approach, the positions of the grains inside the box are more easy to handle as their coordinates are always linked to the box coordinates in this relative moving frame. This solution will also help us to calculate the instantaneous surface angle. The adjustment of this tilting rate has to be controlled according to the real experimental value but also to the ability of the DEM code to handle some "non-static" conditions such as this dynamical tilting studies. When the box angle reaches a value higher than an angle linked to the friction angle of the grains, precursors of avalanches, then local or full avalanches occur. In the real experiments described by Gómez [1], when the box has reached an angle larger than the stability angle, the grains can move and create avalanches. In these avalanches, the grains falled down on the surface of the piling and ended by exiting at the bottom upper side of the box. But, however, in Sect. 5.2.1, we have decided to keep all the grains inside the box. By keeping all the grains, we can assure that we can perfectly control the history of this tilting process. But this fact also implies that the moved grains are still inside the box and have found a new position at the bottom side of the box and naturally created a new top surface. This implies that the consecutive avalanches automatically have a higher angle of stability when the grains have reached a new equilibrium after the previous avalanche. Then in Sect. 5.2.2, we will deal with the case in which beads can leave the box on its top.

4 Preliminary results with dry granular media

In contrary of previous 2D tilting numerical model made by Oger et al. [29] or others authors, no 3D tilting numerical avalanche experiments, in our knowledge, have been done up to now. So, as it is the first numerical study, we have to check the range of available input parameters which can be used and also the list of possibles outputs.

The global stability of any packing of grains depends on the local organization and stability of the contacts surrounding each individual grain. In these contacts, several parameters can influence this characteristic, the stiffness of the grains, their friction coefficient and also their local arrangement due to the geometrical behavior. We will analyze these different effects. In the same manner, we have made several tests by varying the tilting rate in a range varying from 0.25°/s to 12°/s to analyze the process parameters. The sample will be made with glass beads of diameter $D = 1\,\text{mm}$ and density of $2.5\,\text{kg/cm}^3$, the size dispersion is 5 %, the friction coefficient is 0.4, the stiffness is $1.\,10^8\,\text{N/m}$. As described and mentioned in Sect. 3.3 the real experimental values are used to calculate the nondimensional solution of our numerical code where $\tilde{\delta} = \delta/D$ and $\tilde{r} = r/D$ are the nondimensional distances and the dimensionless spring constant $\tilde{k} = k/K_n$. So the weight is equal to $M = \rho h \pi D^2/4 = 1.3\,10^{-3}$ kg and the time scale is of the order of $\sqrt{M/K_n} = 3.6\,10^{-6}$ s which is typically the order of magnitude of the collision between two rigid spheres. We can already notice that, except when specifically mentioned, these values are used in the full section. The fluctuation of some of these mechanical parameters will be analyzed in the following subsections.

Few measurements can be made in order to analyze the evolution of the packing during the tilting process. The first measurement available on the tilting process is the surface slope of the beads. This slope is defined by calculating the best fit of averaged vertical coordinates along the inclination direction. Each vertical coordinate is the mean value of all the spheres perpendicular to the inclination inside a lateral layer and selected close to the surface.

4.1 Size distribution

The local organization of the contacts surrounding one grain is obviously dependent of the diameters of the neighboring grains. For example in a perfect monosize packing a grain can be surrounded by twelve neighbors like in a hexagonal compact structure, otherwise the neighbor value will vary from 4 up to 12 depending of the actual contacts. When the size dispersion increases these mean values can vary a lot and more especially the local value (i.e. a very large grain surrounding by many very small grains). Figure 3 shows the evolution of the slope of the packing made with the same mechanical parameters but with different grain size dispersions. The width of theses dispersions, σ, was varied from 5 to 15 %. Indeed, it is well known that 15 % of diameter disorder is large enough to avoid structured local organizations [32]. The curves present some little difference during the evolution of the slope but the angle for the avalanche remains almost the same. This observation suggests that the local disorder of the contacts do not play a crucial role in the destabilization of the packing during the avalanche.

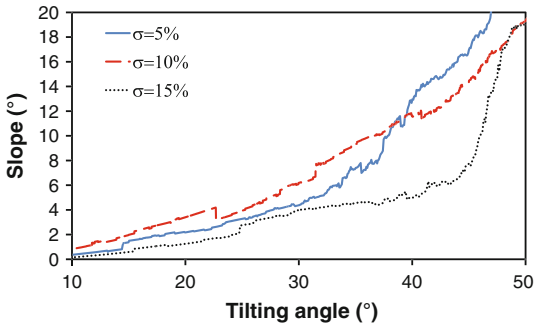

Fig. 3 Slope evolution for different grain size distributions σ. The tilting rate is equal to 2°/s, the friction coefficient equal to 0.4 and the stiffness to 1.10^7 N/m

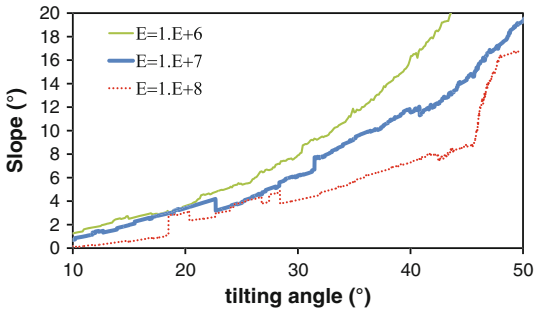

Fig. 4 Slope evolution for different grain stiffness. The tilting rate is equal to 2°/s, the friction coefficient equal to 0.4 and the size distribution to 10%

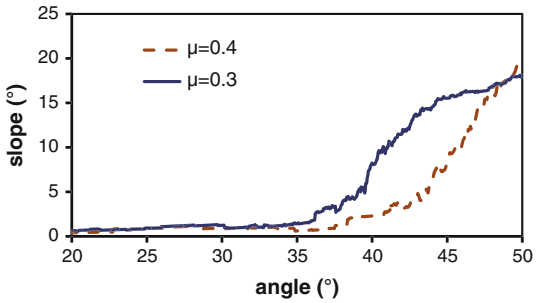

Fig. 5 Slope evolution for different friction coefficients μ. The tilting rate is equal to 2°/s, the stiffness is equal to $1.\,10^8$ N/m and the size dispersion of 5%

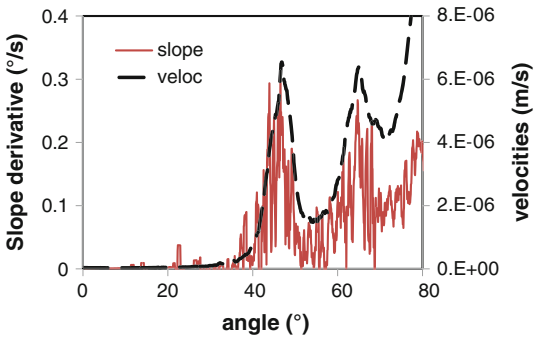

Fig. 6 Comparison of the derivative of the slope and the velocity evolution versus the tilting angle

4.2 Stiffness of the grains

The stiffness of the grains participates in the ability of the packing to be more or less dense by permitting 'adjustable' overlaps between grains. Stiffer grains produce less dense packings. In Fig. 4 we see that the change of the stiffness of the grains has also no significant influence on the evolution of the avalanche. This fact can be easily explain as the grains are mainly static before the avalanche so all their contact interactions are of the same order of magnitude for a given stiffness. This implies that every particle interaction is 'relatively' identical to all of its neighbors.

4.3 Friction coefficient μ

The friction coefficient μ controls, by the Coulomb's law, the local force above which the contact can slip both in the normal or tangential contact interaction. A slipping contact is, of course, a crucial situation when we are looking for precursors of the avalanche and subsequently for the full avalanche itself. This behavior is visible in Fig. 5, which demonstrates the great influence of the local friction coefficient of the grains on the slope for the beginning of the avalanche. We can point out that the angle of the avalanche is much higher than the pure correlation with the friction coefficient ($\theta_s = \arctan(\mu)$). This observation is in perfect agreement with previous experimental results [33]. This difference can be explained by the presence of the walls of the container which keep the grains to start to move at 'low angle'. It is also possible to observe this fact by looking at the summation of all the sphere displacements inside the box.

4.4 Complementary analysis

In Fig. 5 and in the previous paragraph we have already mentioned the possible correlation between the evolution of the slope and the sphere displacements for the same tilting processes. This fact is more visible in Fig. 6 which presents a clear comparison between the fast change for the grain velocities and the change for the surface slope of the packing. So, by looking at this figure, it is obvious that the large displacement of grains can only be seen as an avalanche process. We can already mention that two successive avalanches are shown in the figure and both the velocities and the slope derivative are going down to almost zero. This implies that after the ending of the first avalanche, a waiting situation occurs before the beginning of the second.

4.5 Precursor of an avalanche

As mentioned previously, a lot of experimental studies about the precursors of avalanches were made [33–36]. So another crucial measurement can be done to analyze these avalanche experiments: the apparition of some precursors before the big avalanche. In order to improve our comparison between the real experiments and our numerical model, we have observed the presence of these precursors. In opposition to the experimental point of view which consider two kind of movements: those which involve only few grains (small events) and those which involve a number equivalent to a large part of a grain layer (precursors) and only at the surface layer as part of a precursor event. Instead of dealing with surface displacements we have preferred to use the instantaneous velocities of each sphere as a key measurement. In Fig. 7a we have plotted the global kinetic energy inside the full packing which is more relevant for observing all movements. By comparison with experiments, in Fig. 7b we have presented the kinetic energy for only the spheres on top of the packing which correspond to the spheres observed during the experimental studies.

In the next step, it is important to localize these displacements in the packing and to see if they can be correlated to the standard 'precursors' point of view studied elsewhere [36]. Figure 8 presents the individual velocities of the spheres during the tilting process. Three colors are shown in the figure which correspond to the separation between velocities lower

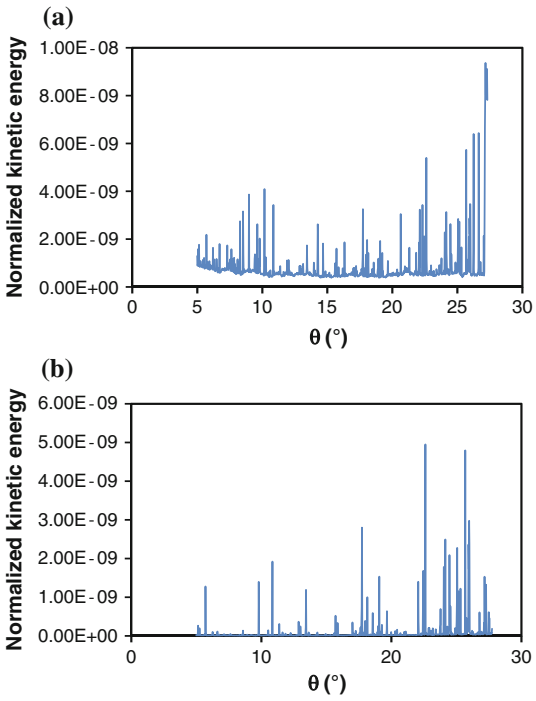

Fig. 7 Analysis of the precursors during the beginning of a tilting process: **a** corresponds to the global measurement and **b** to the surface measurement

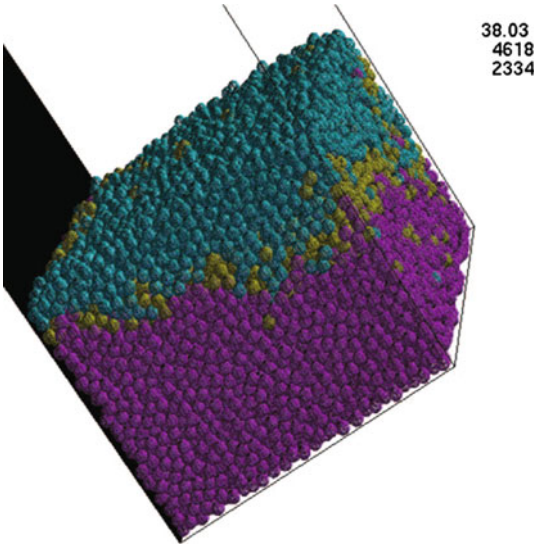

Fig. 8 Representation of the full packing at a tilting angle of 38.03°. The *three colors* correspond to three different sphere instantaneous velocities ranges (*less than* v_1; between v_1 and $2 * v_1$ and *higher than* $2 * v_1$). The legend on the figure represents the tilting angle, and the amount of the spheres having velocities $v_1 = 0.1$ mm/s. (*top*) or $2 * v_1$ (*bottom*) (color figure online)

than $\tilde{v}_1$, velocities between $\tilde{v}_1$ and $\tilde{v}_2 = 2 * \tilde{v}_1$ and velocities higher than $\tilde{v}_2$. In Fig. 8, $\tilde{v}_1$ was chosen equal to $0.4.\,10^{-6}$ which corresponds to a real velocity of 0.1 mm/s. We can notice that the collective position of the spheres having high velocities (i.e. same colors) correspond directly to the volume where the avalanche occurs.

4.6 Intermediate conclusions

Finally, we have demonstrated that our numerical model can handle the classical experiment of 3D tilting box and can generate the expected avalanches with preceding precursor events and followed by successive avalanches. The influence of the friction coefficient and also slightly the effect of the size distribution of the grains have been shown. In contrary, the stiffness of the grains and the tilting rate, in some range of values, does not play a big role in the avalanche process: i.e. no significant difference in the result is found except statistical fluctuations. Now we have a full range of parameters and local and global results coming from tiltings of different packings and histories of packings in order to use them as comparison tools for the insertion of the humidity effect which will be described in the following section.

5 Integration of the humidity effect

5.1 Theoretical considerations

As seen in Sect. 2.1, several models exist to describe the decrease of the adhesion force, linked to the humidity rate,

when the two spheres are moving apart. The two main theories are either an exponential decay [24,26] or a linear model [5]. As the exponential decay does not really define a maximum value after which we can say that no adhesion force exists between the two spheres, we have preferred to use the linear model. In this one, we just have to obtain the maximum value links to f_0 and the slope of the decrease. Now, it is time to quantify these two values according to our experimental setup and Charlaix et al. analysis [5].

Firstly, it is well known that the capillary force depends on the Kelvin's radius r_K and this one is linked to the humidity rate and evolved as shown in Fig. 9a. If we only consider this basic 'geometrical' interaction, we can calculate the spatial contribution which is of the order of 15 nm. If we compared with the range of glass beads used by Gómez [1] which goes from 500 µm up to 2 mm this gives a ratio of $\sim 0.003\,\%$. It is already crucial to note that this interaction is, by comparison, highly smaller than the standard range of possible overlaps obtained in the DEM soft sphere model (typically few %).

As mentioned previously, Charlaix et al. [5] have proposed a very simple model with exact expression to define the adhesion force based on their series of experimental two spheres adhesion tests. In order to show the adaptation of the Charlaix's formula in our case, we have plotted the two key parameters: the maximum adhesion force and the slope when the particles are going apart, versus the humidity rate (Fig. 9b, c). Of course, this extra term concerns the non-overlapping part, in which we assume that the slope starts at the maximum value (f_m) at the end of the overlap of the contact and decreases down to zero. Then f_m follows the equation:

$$f_m = f_0\left(\alpha_0 + \alpha_1\sqrt{r_K} + \alpha_2 * r_K\right) \tag{13}$$

with the three constant values $\alpha_0 = 1, \alpha_1 = -0.555$ and $\alpha_2 = 0.346$ obtained from Crassous et al. [17]. The slope can be expressed as:

$$slope = \frac{f_0}{r_K} \tag{14}$$

In order to have a clear view of the adhesion force versus the distance of two spheres going apart from the pure contact point, we have drawn in Fig. 9d the evolution of this force for two different humidity rates. We cannot observe a big difference for the maximal value of f_m as plotted in Fig. 9b, but we can see a big difference immediately after when δ becomes positive. We can notice that the maximal distance of interaction between two spheres linked by the adhesion term coming from the humidity rate RH is of the order of few percent of the sphere radius (i.e. up to 10 times the hydraulic radius), same order as the overlapping range when δ is negative.

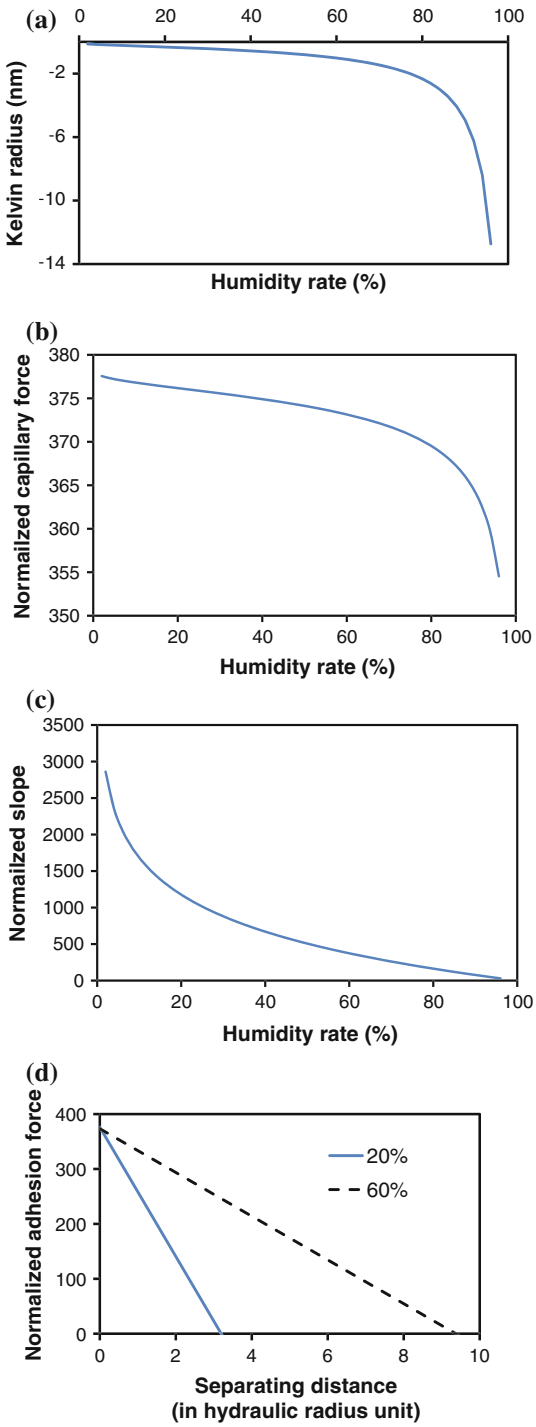

Fig. 9 Calculus of the Kelvin's radius r_K in the geometrical conditions of our experiment with humidity rate (**a**). Maximum value of the adhesion force f_m (**b**) linked to the capillary force f_0 and the humidity rate and the slope decrease (**c**) of this adhesion force with the distance between two spheres versus the humidity rate also. Calculus of the adhesion force versus the separation distance normalized by the hydraulic radius between two spheres for the x axis (**d**). The normalization of the *vertical axis* for (**b**), (**c**), (**d**) are linked to the non-dimensional method of our numerical code described previously

5.2 Preliminary results for humidity rates less than 70 %

5.2.1 Retaining box conditions

We have seen in Sect. 4 which parameters can be relevant for this study and need to be adapted in order to model the avalanche process according to the different mechanical, geometrical and physical inputs which defined this kind of experiments. As some experimental conditions used by Gómez et al. [1] in their analysis are unknown, we have selected relevant values according to the previous results. We used a tilting rate equal to 5°/s with glass beads of diameters 1 mm with a density 2.5 g/cm^3, a restitution coefficient 0.8, a stiffness 1.0 10^8 N/m and a friction coefficient 0.4. All these values will be used in the present section except if specifically mentioned. As already pointed out, the assumption of a possible pendular behavior up to a humidity rate of 70 % will help us to model our sample in some reasonable manner for all this range. We will not present results for higher humidity rates as we already know that our contact model with humidity is not yet able to handle larger adhesion forces due to multiple water filled connected pores.

Figure 10a presents the evolution of the displacement of all the spheres similar to Fig. 5b described in Sect. 4. Figure 10b shows that, at the same time, the slopes of the samples

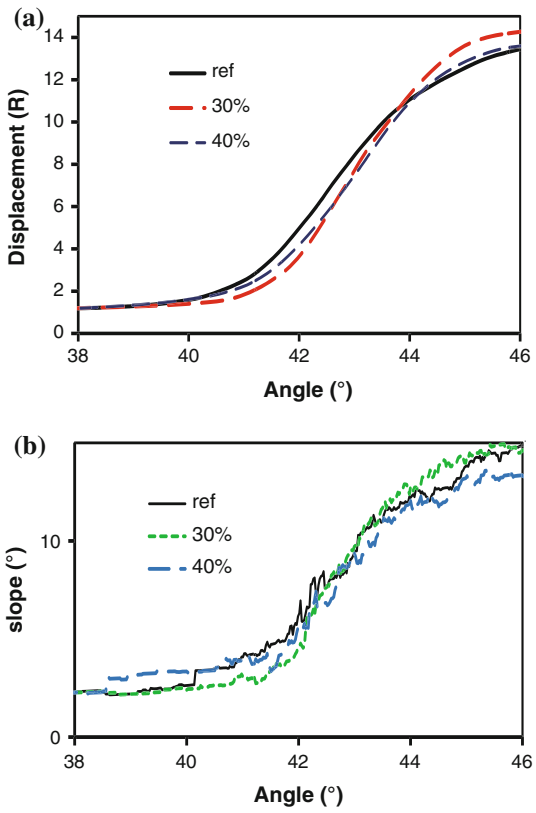

Fig. 10 Displacement and slope evolution for two different humidity rates and comparison with the 'dry' case expressed as 'ref' on the figure

with different humidity rates can have more fluctuations due to any small displacements of the spheres on the surface. In experiments, only these top spheres participate to define the precursors, but in our case we can combine more details by integrating also the inner sphere displacements. This integration tends to smooth the drawing for Fig. 10a.

Indeed, when we are dealing with all the spheres inside the packing, we can understand more easily the 'visible' consequence that is the surface reorganization observed in standard avalanche studies. By knowing that a small group of spheres in the middle of the packing have moved due to a local instability, we can deduce a possible surface reorganization a small delay after. In these humidity cases, the possible appearance of local instabilities is naturally controlled by the number of active contacts (i.e. overlapping contact and those linked by water bridges inside all the packing) surrounding each sphere. More active contacts around one sphere or more stronger ones can decrease the degree of instability. We can also mention that the results of the continuous global displacements of active contacts can imply that, combined with the randomness of the contact distribution evolution, the individual behaviors of the two different packings (30 and 40 %) can present some temporary cases where the direct link between humidity and displacement, slope or contact numbers and humidity rate and tilting angle is not visible. The 40 % can have temporarily higher displacements than the 30 % case. So for this observation, we have plotted in Fig. 11a the evolution of the number of active contacts. We can see that at a given tilting angle, the number of active contacts, before the avalanche, is always higher for 30 and 40 % cases than for 2 % one. In the same manner, on Fig. 11b we can observe that, without adhesion effect, the spheres have a higher mean velocity for the same tilting angle before the avalanche event. This can be explained by a higher probability for some groups of spheres to be involved in precursor events as they are less linked to their neighbors (i.e. less active contact). We can easily see that humidity delays slightly the appearance of the precursors of the avalanche in comparison to the case without any humidity effect. We can also deduce from the previous figures that the angle of the avalanches increases with the humidity rates. The results shown in Fig. 12 are in accordance with Gómez results [1] visible on Fig. 1.

Previously we have assumed that the difference observed for the first avalanche process in the experimental cases can have some links to the special history of the piling of Gómez's experiments [1]: flattening of the upper surface along the box, centers of the upper spheres lower than the border of the box, and so on... it is no more true in our numerical model as the piling is more natural and no screening or surface reorganization is done. So we can easily correlate our results to the evolution also of the second to *n*th avalanches. In these

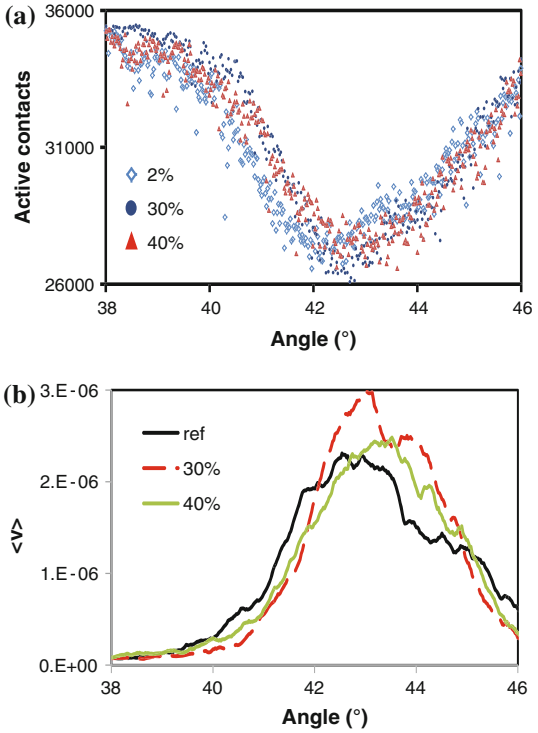

Fig. 11 Number of active contacts for two different humidity rates and comparison with the 'quasi-dry' case (2 %) (**a**). Evolution of the mean velocities of the spheres for two different humidity rates and comparison with the 'dry' case (**b**). *Note:* We have drawn the 2 % case for active contacts plot as the program does not handle active contacts when no humidity is present

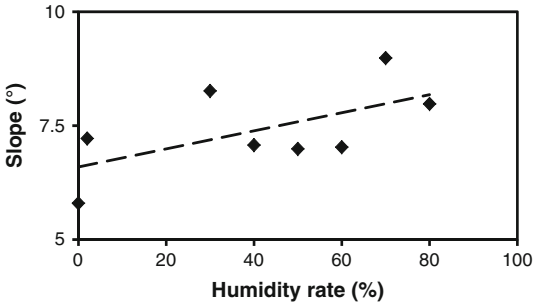

Fig. 12 Evolution of the slope after the avalanche versus the humidity rates. The slope here is only the surface angle difference with the box surface which excluded the inclination angle of the box. This difference explains the smaller range compared to the values of Fig. 1

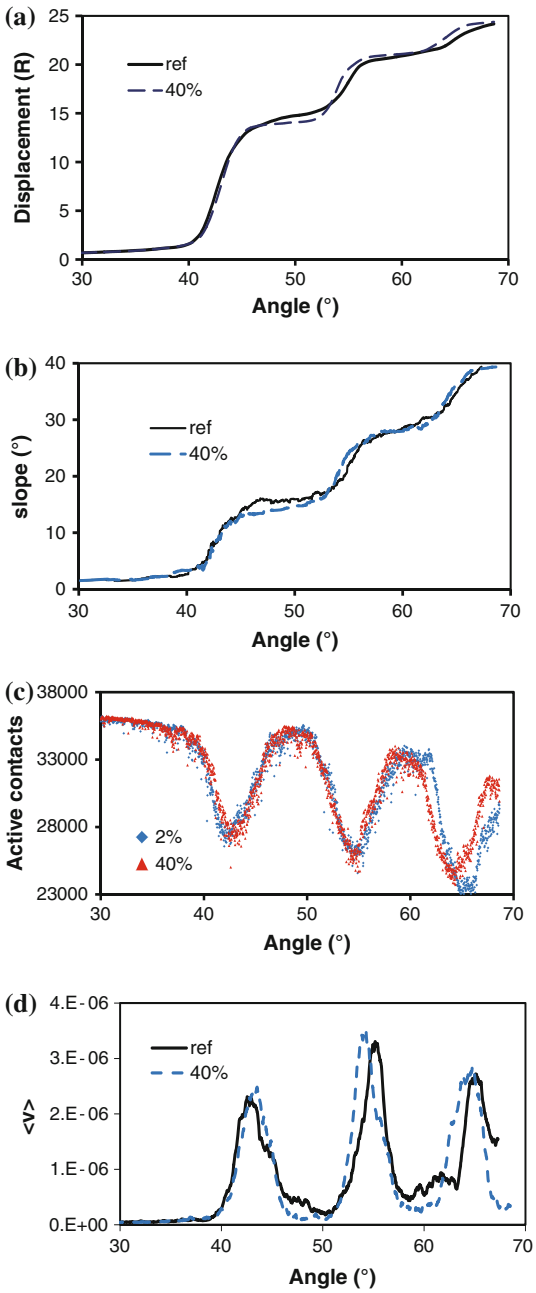

Fig. 13 Slope, displacement, number of active contacts *blue*: 2 % *red*: 40 % and mean velocities of the spheres evolution for a humidity rate of 40 % and comparison with the 'dry' case after several avalanches (color figure online)

cases it was observed a small dependence of the angles on the humidity rates up to 60 % (see Fig. 2) and we can draw the same conclusion here both for the first avalanches and also for the following ones.

In Fig. 13a, b we have also observed the evolution of the successive avalanches in order to see if the experimental behavior observed elsewhere [1] is also valid in our model. We have to notice that, in the experiments, the spheres involved in an avalanche can exit the box by the bottom side, so, in this case, they are no more participating in the rest of the tilting process and surface reorganization. This is not the case in our simulations, as all the spheres are staying inside the box: they can end up at the bottom of the box or participate all along the surface to the new developed surface. This fact conducts to a natural continuous increase of the angles of avalanches and the repose angles for the successive events.

Indeed, we can observe several plateaus either for the displacement behaviors and the slopes which correspond to the

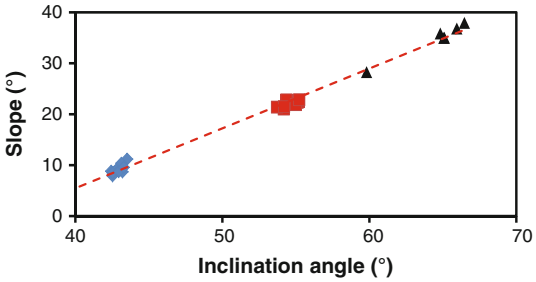

Fig. 14 Evolution of the slope after the successive avalanches for various humidity rates. Each *symbol* corresponds to the same avalanche number. The *dashed line* is the linear fit between all the points. All studied humidity rates from 0 up to 70 % are plotted

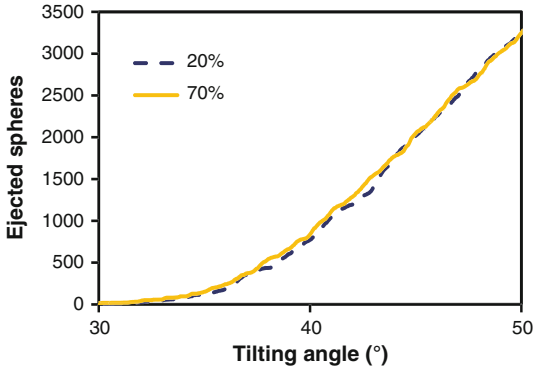

Fig. 15 Evolution of the number of ejected beads versus the tilting angle for two humidity rates. The number of ejected spheres involved in this avalanche increases regularly during the tilting process without showing a plateau after some time

end of one avalanche before the beginning of the following one. In Fig. 13c we have a big decrease of the number of active contacts due to the fast displacements of the spheres during the avalanche, also visible by the high values of the velocities in Fig. 13d. We can see that the velocities are going down to almost zero after these avalanches, which confirm that one avalanche is ended and the new one is not yet in the precursor mode. From another point of view, in Fig. 13c, we can observe that the number of active contacts for the different humidity rates is not completely recovering its previous amplitudes.

This fact is visible in Fig. 14 which shows the evolution of the surface slope due to the cumulative series of avalanches. Even if the successive avalanches are not obviously predictable, the correlation between the slope of each avalanche and the tilting angle where they appeared follow a perfect linear behavior.

5.2.2 Leaving box conditions

In the classical avalanche experiments, the surface of the bead packings is flatten according to the top of the containing box. This fact allows that as soon as one bead start to move significantly, this bead can not be stopped by the bottom of the container and falls naturally outside the box. So it was normal for us to consider this other possible configuration. But, in our case, we cannot flatten perfectly the surface in order to have a clear top of the packing. So we define the upper part of the box where the bead can be eject from the box by the maximal vertical coordinates of the packing (i.e. the highest center of the beads plus its radius). We can mention that this value can already be seen as higher than the configuration case of the experiments.

This non reorganization of the top of our packing can also permit us to say: as already mentioned, it is important to notice that we have not created an initial local dense structure due to the pushing of some top beads during the adjustment of the surface. This allows us to admit that the first avalanche can be similar to the following ones in opposition to the experimental cases, where we suppose that the origin of the first avalanche is linked to either the dense flattening process of the experiment or the perfect arrangement of the upper layer compared to the box height. This is the goal of this part.

This new experimental condition implies naturally that a lot of displacements of beads during an avalanche can produce displacements large enough to let the beads falling outside the box. But even if in the real experiments we can say that the avalanche appears suddenly and the displacements of the beads outside the container are also very rapid, from the numerical point of view, the code needs some time in order to count the beads going out. To achieve this, the time evolution of the simulation has to be very very slow, that is not possible in a reasonable computer time. In practice the beads are moving continuously as seen here. In Fig. 15 we have plotted the evolution of the number of ejected beads during the avalanche phase for humidity rates of 20 and 70 %. We can observe that the number of ejected spheres involved in this avalanche increases regularly during the tilting process without showing a plateau after some time. This big difference with experiments is not yet perfectly understood but can be partially explained by the remaining granular temperature inherent of the classical DEM code which cannot permit to slow down enough the sphere already involved in some displacements.

By opposition to Fig. 15 where we were unable to see the influence of the humidity rates, we have plotted in Fig. 16 the evolution of the number of ejected spheres versus the total number of spheres which have moved during the tilting process. This figure confirms that less spheres inside the packing have participated at the surface slipping up to the exit when the humidity rate is high. This is consistent with the fact that a higher adhesion force between spheres helps to maintain more of them immobile.

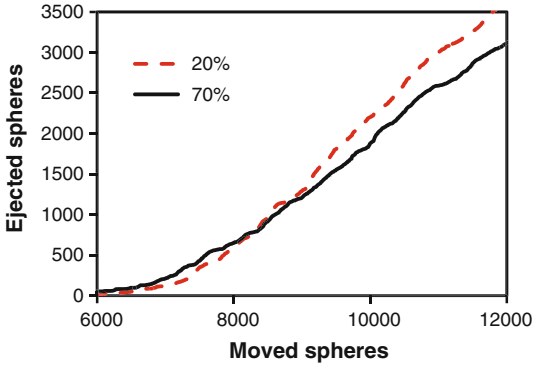

Fig. 16 Evolution of the ejected moved spheres versus the total number of spheres which have moved during the same time for two humidity rates (20 and 70 %)

6 Conclusions

We have demonstrated that our numerical simulation can handle the full process of avalanching during continuous slow tilting experiments. We have presented a clear correlation between the fast change of the grain velocities and the change of the surface slope of the packing. So, even if we were dealing with a 'quasi-static' DEM model, we can admit that the large displacement of grains can only be seen as an avalanche process. We have used the theoretical model developed by Charlaix et al. [5] to define and implement the adhesion force inside our model. Up to an humidity rate of 70 %, we can say that our assumption about pendular environment seems to work quite well. But it is clear that higher humidity rates will imply more complex grain to grain interactions. This interaction will have to include several neighboring contacts in order to mimic the funicular and maybe the capillary state.

Acknowledgments L. Oger would like to thanks the Universidad Nacional de San Luis for the one month invitation as invited professor. A.M. Vidales, R.O. Uñac. and I. Ippolito want to thank CONICET support through the grant PIP No. 1022. We thanks Jean Pierre Hulin for fruitful discussions. This work is partially supported by the LIA *Physique et Mécanique des Fluides*.

References

1. Gómez, I., Ippolito, I., Chertcoff, R.: Characterization of wet granular media behaviour under diferent relative humidity conditions. Powder Technol. submitted (2012)
2. Mitarai, N., Nori, F.: Wet granular materials. Adv. Phys. **55**(1–2), 1–45 (2006)
3. Charlaix, E., Crassous, J.: Adhesion forces between wetted solid surfaces. J. Chem. Phys. **122**, 184701 (2005)
4. Richefeu, V., el Youssoufi, M.S., Radjaï, F.: Shear strength properties of wet granualr materials. Phys. Rev. E **73**, 051304 (2006)
5. Charlaix, E., Ciccotti, M.: Chap. 12 capillary condensation in confined media. In: Sattler, K.D. (ed.) Handbook of Nanophysics: Principles and Methods. CRC Press, Boca Raton (2010)
6. Herminghaus, S.: Dynamics of wet granular matter. Adv. Phys. **54**(3), 221–261 (2005)
7. Schulz, M., Schulz, B.M., Herminghaus, S.: Shear-induced solid-fluid transition in a wet granular medium. Phys. Rev. E **67**, 052301 (2003)
8. Iveson, S., Wauters, P., Forrest, S., Litster, J., Meeters, G., Scarlett, B.: Growth regime map for liquid-bound granules: further development and experimental validation. Powder Technol. **117**, 83–97 (2001)
9. Hornbaker, D.J., Albert, R., Albert, I., Barabasi, A.L., Schiffer, P.: What keeps sandcastles standing? Nature **387**, 765 (1997)
10. Kohonen, M.M., Geromichalosb, D., Scheelb, M., Schierb, C., Herminghaus, S.: On capillary bridges in wet granular materials. Phys. A **339**, 7–15 (2004)
11. Tegzes, P., Albert, R., Paskvan, M., Barabasi, A., Vicsek, T., Schiffer, P.: Liquid-induced transitions in granular media. Phys. Rev. E **60**(5), 5823–5826 (1999)
12. Forny, L., Pezron, I., Guignon, P., Kounjer, L.: Peculiar absorption of water by hydrophobized glass beads. Coll. Surf. A: Physicochem. Eng. Aspects **270–271**, 263–269 (2005)
13. Crassous, J., Charlaix, E.: Nanoscale investigation fo wetting dynamics by a surface force apparatus. Phys. Rev. Lett. **78**, 2425–2428 (1997)
14. Bocquet, L., Charlaix, E., Castagno, F.: Physics of humid granular media. Phys. C.R. **3**, 207–215 (2002)
15. Restagno, F., Crassous, J., Cottin-Bizonne, C., Charlaix, E.: Adhesion between weakly rough beads. Phys. Rev. E **65**, 042301 (2002)
16. Restagno, F., Bocquet, L., Crassous, J., Charlaix, E.: Slow kinetics of capillary condensation in confined geometry: experiment and theory. Coll. Surf. A: Physicochem. Eng. Aspects **206**, 69–77 (2002)
17. Crassous, J., Ciccotti, M., Charlaix, E.: Capillary force between wetted nanometric contacts and its application to atomic force microscopy. Langmuir **27**, 3468–3473 (2011)
18. Gómez, I.: Caracterizacion higroscopica de materiales de construccion: arcilla aligerada y picon. Ph.D. thesis, Universidad del Pais Vasco (2006)
19. Lian, G., Thornton, C., Adams, M.J.: Discrete particle simulation of agglomerate impact coalescence. Chem. Eng. Sci. **53**(19), 3381–3391 (1998)
20. Dong, K., Yand, R., Zou, R., Yu, A.: Role of interparticle forces in the formation of random loose packing. Phys. Rev. Lett. **96**, 145505 (2006)
21. Dong, K., Yand, R., Zou, R., Yu, A.: Settling of particles in liquids: effects of material properties. A.I.Ch.E. **58**(5), 1409–1421 (2012)
22. Yu, A., Feng, C., Zou, R., Yang, R.: On the relationship between porosity and interparticle forces. Powder Technol. **130**, 70–76 (2003)
23. Richefeu, V., el Youssoufi, M.S., Azéma, E., Radjaï, F.: Force transmission in dry and wet granualar media. Powder Technol. **190**, 258–263 (2009)
24. Soulié, F., Cherblanc, F., Youssoufin, M.S.E., Saix, C.: Influence of liquid bridges on the mechanical behaviour of polydisperse granular materials. Int. J. Numer. Anal. Meth. Geomech. **13**, 213 (2006)
25. Anand, A., Curtis, J.S., Wassgren, C.R., Hancock, B.C., Ketterhagen, W.R.: Predicting discharge dynamics of wet cohesive particles from a rectangular hopper using the discrete element method (dem). Chem. Eng. Sci. **64**, 5268–5275 (2009)
26. Mikami, T., Kamiya, H., Horio, M.: Numerical simulation of cohesive powder behavior in a ßuidized bed. Chem. Eng. Sci. **53**(10), 1927 (1998)
27. Walton, O.R., Braun, R.L.: Viscosity, granular-temperature, and stress calculations for shearing assemblies of inelastic, frictional disks. J. Rheol. **30**(5), 949–980 (1986)

28. Savage, S.B.: Disorder diffusion and structure formation in granular flows. In: Bideau, D. (ed.) Disorder and Granular Media, pp. 255–287. North Holland, Amsterdam (1993)
29. Oger, L., Ippolito, I., Vidales, A.: How disorder can diminish avalanche risks: effect of size distribution. Granul. Matter **9**, 267–278 (2007)
30. Powell, M.J.: Computer-simulated random packing of spheres. Powder Technol. **25**, 45–52 (1980)
31. Janssen, H.A.: Versuche über Getreidedruck in Silozellen. Zeitschr. d. Vereines deutscher Ingenieure **39**(35), 1045–1049 (1895)
32. Lochmann, K., Oger, L., Stoyan, D.: Statistical analysis of random sphere packings with variable radius distribution. Solid State Sci. **8**, 1397–1413 (2006)
33. Mint Babah, H.: Etude expérimentale de quelques aspects de la problématique des dunes éoliennes: des processus d'avalanche à la statigraphie des dunes. Ph.D. thesis, University of Rennes 1 (2010). http://www.sudoc.fr/146157036
34. Nerone, N., Aguirre, M., Calvo, A., Ippolito, I., Bideau, D.: Surface fluctuation in a slowly driven granular system. Phys. A **283**, 218–222 (2000)
35. Nerone, N., Aguirre, M., Calvo, A., Bideau, D., Ippolito, I.: Instabilities in slowly driven granular packing. Phys. Rev. E **67**, 011302 (2003)
36. Kiesgen de Richter, S., Le Caër, G., Delannay, R.: Dynamics of rearrangements during inclination of granular packings: theavalanche precursor regime. J. Stat. Mech. p. 04013 (2012)